Journal of Alloys and Compounds 1036 (2025) 181964

Contents lists available at ScienceDirect

Journal of Alloys and Compounds

journal homepage: www.elsevier.com/locate/jalcom

Tuning magnetocaloric effect of Tb-based amorphous alloy by powder size and hydrogenation

Qianzi Yang, Qiang Luo *, Jingxian Cui, Mingjie Zhang, Haoyang Chang, Haoran Zhou, Yao Zhang, Baolong Shen *

School of Materials Science and Engineering, Jiangsu Key Laboratory for Advanced Metallic Materials, Southeast University, Nanjing 211189, China

ARTICLE INFO

Keywords:
Magnetocaloric materials
Magnetic refrigeration
Amorphous alloys
Dual-phase alloy
Hydrogenation

ABSTRACT

Amorphous alloys are garnering increasing attention as promising candidates for magnetic refrigerants. However, their low to medium magnetic entropy changes pose challenges for practical applications, and the relationship between structural heterogeneity and magnetocaloric performance remains poorly understood. In this work, the influences of structure order and nanoscale hydride formation on the magnetocaloric effect (MCE) of $Tb_{55}Co_{20}Al_{24}Si_1$ amorphous alloy powders are investigated. The degree of structure order tuned by particle size plays a significant impact on the MCE, and the powders with medium degree of structure order present the largest maximum magnetic entropy change of 7.5 J $kg^{-1}K^{-1}$ under 5 T. After formation of nanoscale hydride by hydrogenation, the predominant exchange coupling of the alloy is transformed from ferromagnetic to antiferromagnetic interaction, accompanied by the disappearance of spin-glass-like freezing behavior. Significantly, the maximum magnetic entropy change further increases to 13.2 J $kg^{-1}K^{-1}$ under 5 T, representing an increase of 56.8 %, and the coercivity shows a considerable reduction. These findings suggest that TbCoAlSiH dual-phase alloy holds promise as a novel magnetic refrigeration material at low temperatures.

1. Introduction

Refrigeration technology plays a crucial role in space science and technology, large-scale air conditioner, gas liquefaction, chemical processing, and so on. In contrast to the traditional gas refrigeration technology, magnetic refrigeration technology offers environmental friendliness, pollution-free operation, and high refrigeration efficiency [1–3]. Therefore, increasing attention has been focused on the development of various magnetic materials exhibiting advanced magnetocaloric properties [4–12]. Among magnetocaloric materials, the crystalline alloys with first-order magnetic transition (FOMT) (such as La-Fe-Si, Gd-Si-Ge) may possess giant magnetic effects [13–16], indicating their potential as magnetic refrigerants. However, they often exhibit magnetic and/or thermal hysteresis, brittleness, and narrow magnetic entropy change peak, limiting their practical application. Recently, amorphous alloys (AMAs) with second-order magnetic transition (SOMT) are garnering increasing attention, due to their free of magnetic/thermal hysteresis, high electronic resistance resulting in reduced eddy current losses, and broad magnetic entropy peak leading to large refrigeration capability (RC) [17,18]. Nevertheless, their medium magnetic entropy changes, which are obviously inferior to those of typical crystalline alloys with FOMT [19–21], have been a long-standing shortcoming of amorphous alloys as promising magnetic refrigerant.

Recently, the introduction of nanocrystals in the amorphous matrix has been used to enhance the magnetocaloric effect (MCE) in some rare earth-based amorphous alloys [22,23]. Xia *et al.* discovered that the presence of precipitated grains enhanced the magnetocaloric properties of a Gd-based metallic glass [24]. Du *et al.* utilized a rapid quenching technique to directly fabricate nanocrystalline dual-phase alloy. The maximum magnetic entropy reached 7.8 J $kg^{-1}K^{-1}$ under 5 T, with a magnetic refrigeration capacity of 551 J kg^{-1} [25]. Sun *et al.* demonstrated that current annealing induced nanocrystals in GdTbCoAlFe metallic glass fibers broadened the refrigeration temperature region and enhanced the RC [26]. Huo *et al.* synthesized GdNiAl amorphous/nanocrystalline composite microfilaments with a magnetic refrigeration capacity of 985 J kg^{-1}, suggesting the potential application of metallic glass composites in the near-room-temperature region [27]. Besides, an obvious enhancement of the maximum magnetic entropy change (under 5 T) from 9.5 J $kg^{-1}K^{-1}$ to 10.7 J $kg^{-1}K^{-1}$ was achieved through

* Corresponding authors.
E-mail addresses: q.luo@seu.edu.cn (Q. Luo), blshen@seu.edu.cn (B. Shen).

https://doi.org/10.1016/j.jallcom.2025.181964
Received 21 November 2024; Received in revised form 27 June 2025; Accepted 29 June 2025
Available online 30 June 2025

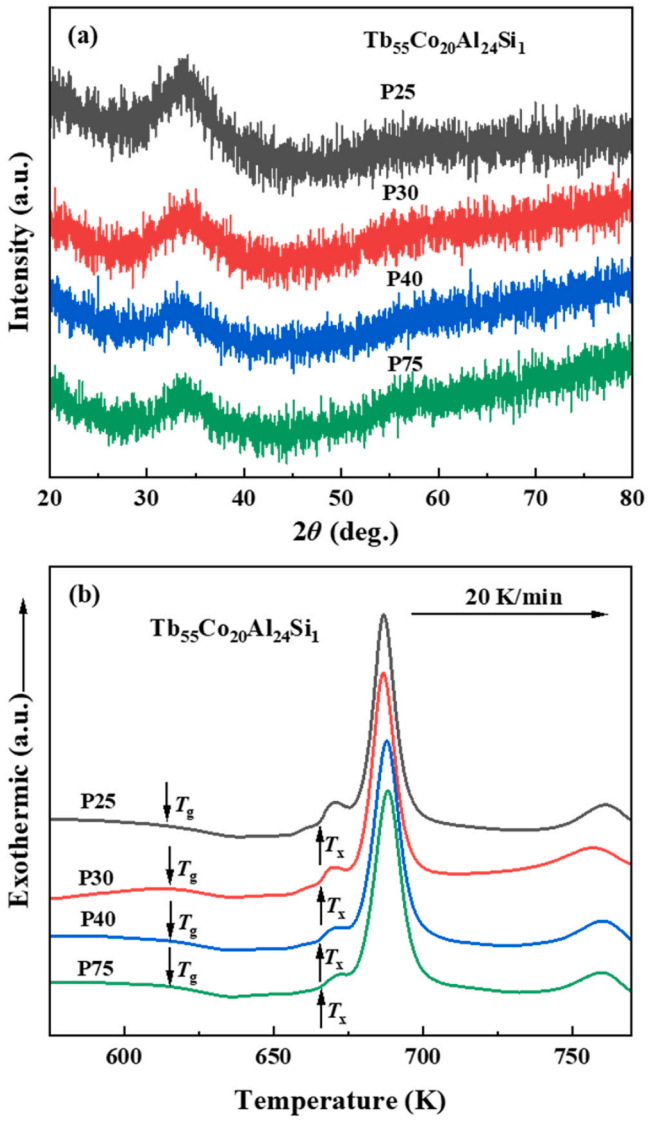

Fig. 1. (a) XRD patterns of $Tb_{55}Co_{20}Al_{24}Si_1$ amorphous alloy powder with four grain sizes. The inset shows the SEM image of the P30 sample. (b) DSC curves of four grain size of $Tb_{55}Co_{20}Al_{24}Si_1$ amorphous alloy powder.

modulation of the local structure via cryogenic thermal cycling treatment [28]. Nevertheless, the improvement of $-\Delta S_M^{max}$ by precipitating these nanocrystals is limited in magnitude, and in many cases, (nano) crystallization by annealing deteriorates the MCE performance of AMAs [29]. In addition, the majority of these studies have concentrated on Gd-based AMAs, primarily because of their magnetic softness across the entire temperature range under investigation. Other heavy rare earth-based (such as Dy-, Tb-, Ho-, Er-based) AMAs have large magnetic hysteresis below the spin freezing temperature [30], which makes them less attractive. Simultaneously enhancing the MCE and magnetically softening these rare earth-based AMAs with large magnetic hysteresis remain a longstanding challenge.

$Tb_{55}Co_{20}Al_{24}Si_1$ composition was chosen due to its large glass forming ability and large magnetic moment of the Tb atom [31]. Here, we prepared $Tb_{55}Co_{20}Al_{24}Si_1$ amorphous alloy powders and explored the effects of degree of local structure order (tuned by powder size) and nanoscale hydride formation on their MCE performance. It is revealed that powders (25–30 μm in diameter) with medium degree of local structure order present the largest maximum magnetic entropy change of 7.5 J $kg^{-1}K^{-1}$ (5 T) among the powders with different powder size ranges. After hydrogenation, unique dual-phase structure with nano-sized hydrides in the residual amorphous phase is obtained. This amorphous/nanocrystalline dual-phase alloy TbCoAlSiH shows distinctive enhancement of the maximum magnetic entropy change from 7.5 J $kg^{-1}K^{-1}$ to 13.2 J $kg^{-1}K^{-1}$ under 5 T and significantly improved the magnetic softness. The correlation between dual-phase structure and MCE properties is clarified.

2. Experimental section

$Tb_{55}Co_{20}Al_{24}Si_1$ master alloy was prepared by arc-melting in an argon atmosphere using a mixture of pure Tb, Co, Al, and Si. The purity of the Tb element was better than 99.9 %, and the purity of the Co, Al, and Si elements was better than 99.99 wt%. Four types of amorphous powders with particle sizes of < 25 μm, 25–30 μm, 30–40 μm, and 40–75 μm were prepared by gas atomization method. The hydrogenated sample powders were obtained by isothermal hydrogenation experiments at a holding temperature of 200 ℃ with a hydrogen gas pressure of 5 MPa in a Sieverts-type apparatus (Advanced Materials Corporation, No. 0360Q). The as-prepared samples at different particle sizes of < 25 μm, 25–30 μm, 30–40 μm, and 40–75 μm, and the hydrogenated treated sample are denoted as P25, P30, P40, P75, and H30, respectively.

The structure of the powders was characterized by Cu-Kα radiation x-ray diffraction (XRD, Rigaku SmartLab9k). The high-resolution transmission electron microscopy was characterized by transmission electron microscopy (TEM, Talos F200X). High-angle annular dark field (HAADF) images were recorded using a probe semi-convergence angle of 10.5 mrad and collection semi-angle of 72–200 mrad. Elemental mappings of the samples were acquired by energy-dispersive spectroscopy (EDS). Samples for TEM studies were prepared by Focused Ion beam (FIB). The morphology of the powders was characterized by scanning electron microscopy (SEM, FEI Sirion 200). The glass transition temperature T_g and crystallization temperature T_x were obtained using differential scanning calorimetry (DSC, NetzschDSC404F3) at a heating rate of 20 K/min. The temperature and field dependence of DC magnetization was measured using a SQUID magnetometer (MPMS, Quantum Design). The 2D maps of the reduced elastic modulus (Er) with a spacing of 1 × 1 $μm^2$ on the surface of samples were performed by atomic force microscopy (AFM, bruker).

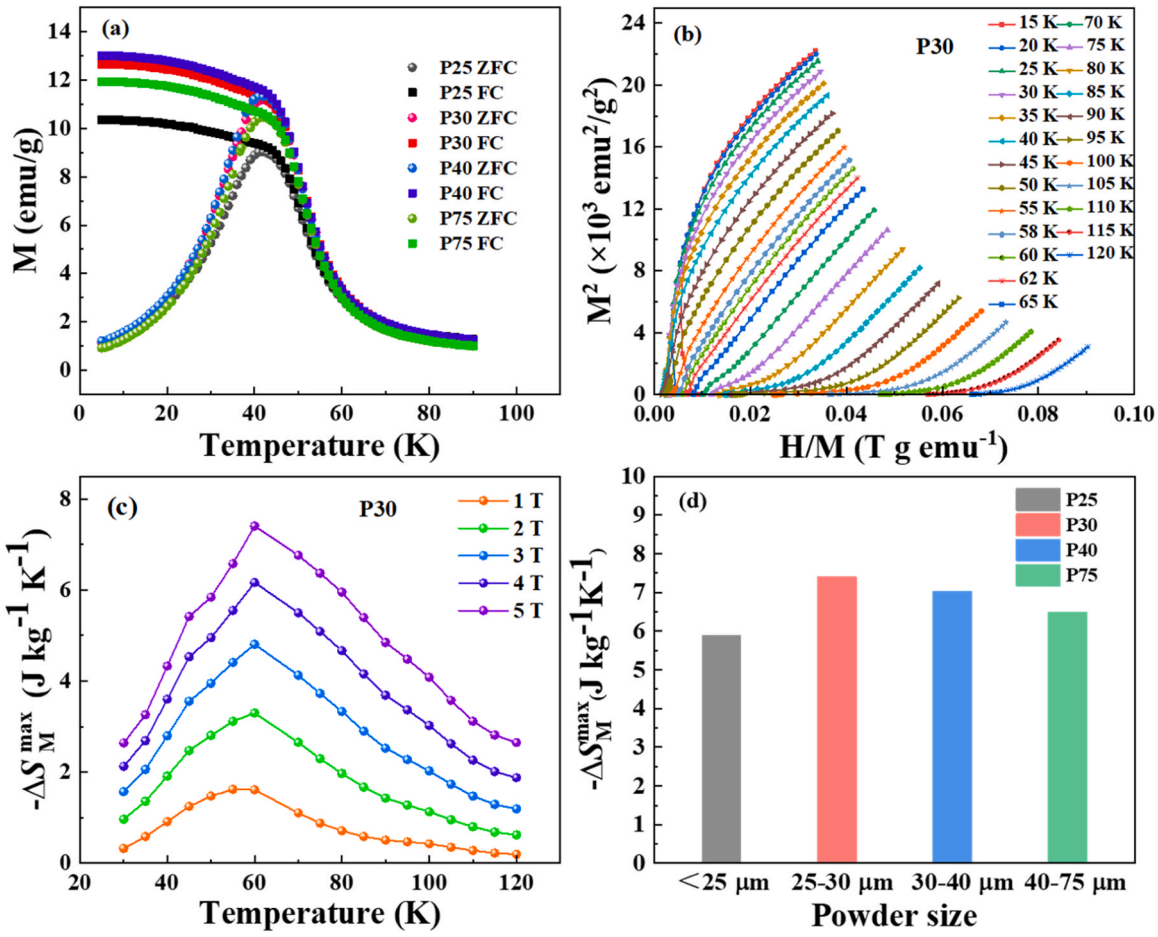

Fig. 2. (a) Magnetization curves of $Tb_{55}Co_{20}Al_{24}Si_1$ amorphous alloy powders with four grain sizes. (b) Arrott plots calculated from *M–H* curves of the P30 sample. (c) Temperature dependence of ΔS_M of the P30 sample under the maximum applied field from 1 to 5 T.(d) Temperature dependence of ΔS_M versus grain size.

3. Results and discussion

3.1. The effect of particle size on the magnetocaloric properties

Fig. 1(a) shows the XRD patterns of the $Tb_{55}Co_{20}Al_{24}Si_1$ powders with different sizes. There is only a diffuse scattering hump near 2θ of 34° without obvious crystallization diffraction peaks, indicating their amorphous structure. As shown in the inset of Fig. 1(a), the P30 powders exhibit good sphericity. Fig. 1(b) presents the DSC curves of the $Tb_{55}Co_{20}Al_{24}Si_1$ powders, showing clear glass transition and crystallization events. The T_g of the P25, P30, P40 and P75 samples are determined to be 614, 615, 615 and 613 K, respectively. And the T_x of those samples are measured to be around 665 K. Although having similar T_g and T_x, the shapes of the crystallization peaks (around 686 K) show obvious difference, indicating the variation of the local structures with changing powder size.

Fig. 2(a) shows the field cooled (FC) and zero field cooled (ZFC) magnetization curves of the $Tb_{55}Co_{20}Al_{24}Si_1$ powders. The FC curve was measured after cooling the sample to 5 K under 200 Oe, and the ZFC curve after cooling under zero Oe. From the FC curve, the Curie temperature T_c corresponding to the differential of the magnetization curve can be determined to be ~50 K for all the powders with different sizes. And similar spin-freezing temperatures (T_f) around 40 K are observed for all the powders, near where the ZFC and FC curves show bifurcations. The spin glass-like behavior is related to the strong random magnetic anisotropy originating from the Tb atoms [31]. It is noted that magnetization values near the spin freezing temperature vary obviously with the powder size and tend to approach the same values when

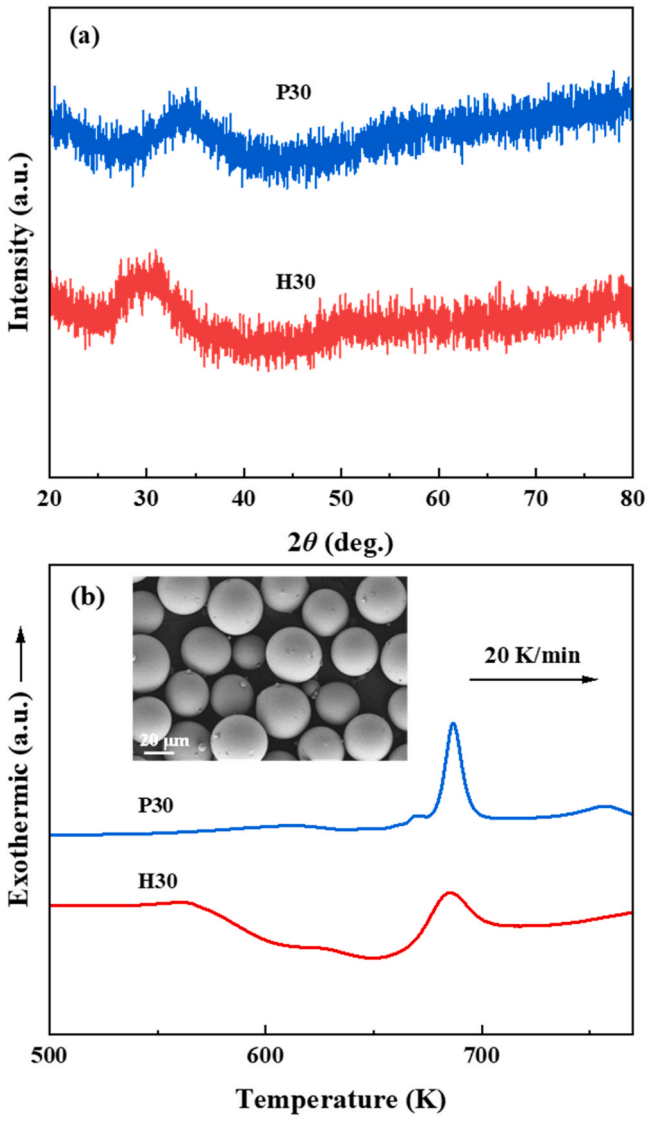

Fig. 3. (a) X-ray diffraction comparison of the P30 and H30 samples. (b) DSC curves of the P30 and H30 samples. The inset shows the SEM images of the H30 sample.

moving away from the spin freezing temperature. Since all the powders are amorphous, the change of the magnetization feature near T_f with powder size arises from the variation of the local structures [32]. To illustrate the magnetic transition type of the powders, the typical Arrott curves for P30 are shown in Fig. 2(b). At 15 K and 20 K, due to the spin-glass-like behavior of $Tb_{55}Co_{20}Al_{24}Si_1$, the Arrott plot has a negative slope [33]. At high temperatures above 25 K, the slopes of the Arrott plots for the P30 sample are all positive, indicating that the $Tb_{55}Co_{20}Al_{24}Si_1$ powders show a secondary magnetic transition [34]. Similar features are observed for all other powders.

The maximum magnetic entropy change is one of the most important parameters to evaluate magnetocaloric performance of magnetic materials. Based on the isothermal *M-H* curves, the temperature dependence of magnetic entropy change of P30 shown in Fig. 2(c) was determined by Maxwell's equations:

$$\Delta S_M(T,H) = S_M(T,H) - S_M(T,0) = \int_{H_0}^{H_{max}} \left(\frac{\partial M}{\partial T}\right) dH \quad (1)$$

The sample reaches a maximum magnetic entropy ($-\Delta S_M^{max}$) of 7.5 J $kg^{-1}K^{-1}$ under a 5 T near the Curie temperature T_c. This maximum value is slightly smaller than those of the Gd-based AMAs but larger than those of the Fe-based AMAs [35,36]. The peak temperature and shape of the curves remain almost the same under different field variations, and just the values decrease with decreasing field. Fig. 2(d) compares the -ΔS_M under a field change of 5 T for the four groups of powders with different sizes. The maximum -ΔS_M is smallest for the P25 powders, and largest for the P30 powders. The different $-\Delta S_M^{max}$ values come from their different local structures. A particle with larger/smaller size has a slower/faster cooling rate and take a longer/shorter time to rearrange the structure to reach a more ordered state. This implies that the larger power has a larger fraction of short-to-medium range ordered local structures. Fig. 2(d) indicates that moderate degree of structural order may be beneficial for enhancing MCE of AMAs. This is according with previous findings in Fe-based AMAs and Gd-based bulk AMAs [30].

3.2. Hydrogenation and microstructure analysis

Then we chose P30 powders to further modify the local structure and MCE by hydrogenation. Fig. 3(a) compares the XRD patterns of the P30 powders and the H30 powders. Consistent with the P30 powders, the hydrogenated sample's XRD pattern also exhibits no discernible crystallization peaks, suggesting the material retains its amorphous nature within XRD detection limits. However, the potential existence of nanocrystallites (1–3 nm) with a relatively low volume fraction cannot be excluded. Besides, the diffuse scattering humps corresponding to the amorphous structure shift leftward to lower angles after hydrogen absorption, suggesting an increase in the average atomic distance of the amorphous matrix. This is consistent with the previous results reported in hydrogenated metallic glasses [29,37,38]. According to the anionic theoretical model, after the hydrogen absorption, electrons are transferred from the conduction band to the hydrogen 1 s shell layer [39], leading to a decrease in the number of electrons involved in the Ruderman–Kittel–Kasuya–Yosida (RKKY) interaction. However, the strong affinity between hydrogen and Tb necessitates consideration of potential nanoscale hydride precipitates. The DSC curves of the P30 and H30 powders are comparatively shown in Fig. 3(b). After hydrogen absorption, an obvious crystallization peak is still observed, but the intensity of the crystallization peak is reduced, indicating the existence of some nanocrystalline phase embedded in the amorphous matrix. The onset of glass transition cannot be determined due to the overlap between the glass transition and broad endothermic events. The broad endothermic peak between 560 K and 650 K arising from the hydrogen release further indicates the formation of hydride in the amorphous matrix of the H30 alloy. The inset of Fig. 3(b) shows the SEM image of the H30 powders, indicating good sphericity.

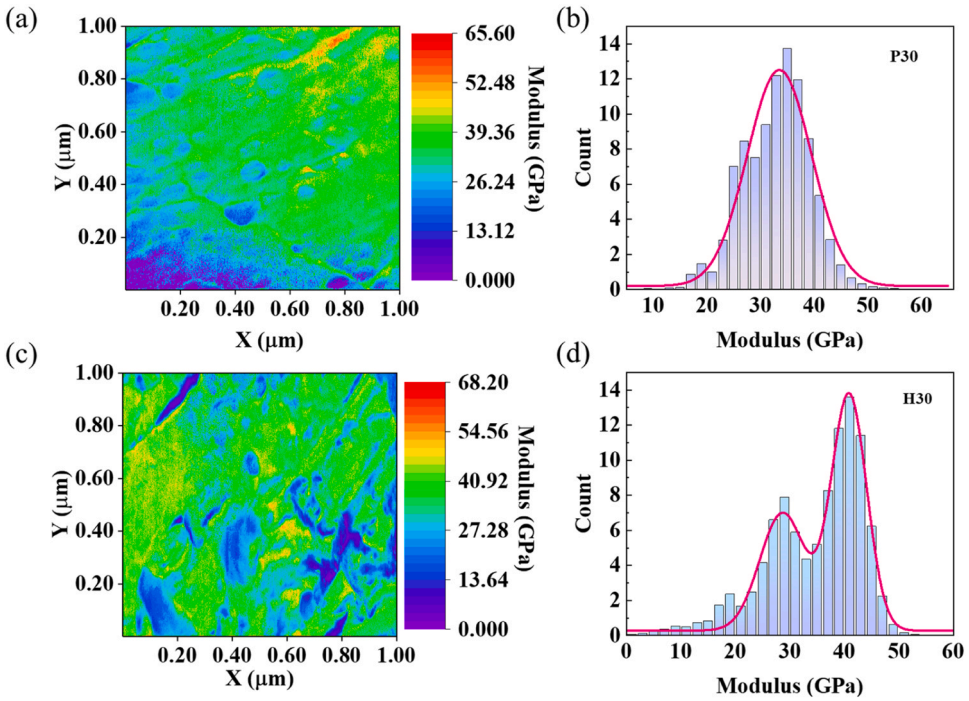

Fig. 4. (a) Mapping of local reduced modulus for the samples (a) the P30 sample, (b) the H30 sample. (c-d) The corresponding statistical distribution of local reduced modulus for the samples (c) the P30 sample, (d) the H30 sample.

To acquire the local mechanical properties of the P30 and H30 samples and illustrate the dual phase structure, nanoindentation experiments were performed in an area of 1×1 μm^2 on the surface of samples. The reduced elastic moduli (E_r) of the P30 and H30 sample are shown in Fig. 4(a) and (b), from which a more heterogeneous microstructure can be seen clearly in H30. To show their difference of spatial heterogeneity more clearly, the corresponding statistical distribution curves of E_r for the P30 and H30 samples are obtained, and both can be fitted by Gaussian function very well (Fig. 4(c) and (d)). The P30 sample demonstrates a maximum in the reduced elastic modulus at 40 GPa, with values ranging from 4.2 to 65.5 GPa. In contrast, the H30 sample exhibits two peaks at approximately 29 and 40 GPa, with the modulus ranging from 1.7 to 68.2 GPa, implying its dual-phase structure. To further show the atomic structure, the HRTEM image of the H30 sample is presented in Fig. 5(a). Fig. 5(b) is an enlarged view of the white square in Fig. 5(a). The local structure orders on a scale of 1–3 nm can be seen in white squares, whereas other regions show amorphous structure with random atomic arrangement. Combing the results of the broad endothermic event before crystallization in the DSC curve, ac magnetic susceptibility (see below), and dual-phase distribution of modulus, it is reasonable to argue that these nanocrystals should be rare earth hydrides [40]. In addition, the elemental mappings of the H30 sample in Fig. 5(d-h) show that Tb, Co, Al, Si elements are uniformly distributed and there is no obvious elemental segregation in the H30 sample.

3.3. Effect of nanosized hydrides on magnetocaloric properties

Fig. 6(a) shows the ZFC and FC curves of the H30 sample under a field of 0.02 T. Although a ZFC peak is not observed, the ZFC and FC curves begin to diverge around 10 K. The $1/\chi(T)$ curve for the H30 sample obeys the Curie–Weiss law at high temperature region ($\chi(T)=C/(T-\theta_P)$). The paramagnetic Curie temperature of the H30 sample is obtained as −17 K as shown in the inset of Fig. 6(a), which implies that the dominant exchange interaction after hydrogen absorption is antiferromagnetic (from Terbium hydrides). It is known that Tb has a high chemical affinity for hydrogen, readily forming hydrides with antiferromagnetic ordering at low temperature. As documented by BOS, the Néel temperature of TbH_2 is 46 K [41]. In the case of TbCoAlSiH, its Néel temperature is lower than that of TbH_2. This is attributed to the presence of amorphous layers that separate the TbH_2 nanoclusters from the matrix, thereby influencing the magnetic interactions. Smilar antiferromagnetic ordering from rare earth hydrides has been observed in GdTbDyCoAl amorphous alloy [40]. To evaluate the effect of hydrogenation on magnetic transition and magnetic entropy change, the isothermal magnetization curves of the H30 sample were measured and are shown in Fig. 6(b). Different from the P30 sample, the crossing behavior arising from the spin-glass-like behavior is not observed in the *M-H* curves of the H30 sample, indicating the different magnetic transition nature of H30. The Arrott curves of the H30 powders are shown in Fig. 6(c). The slopes of the Arrott plots are positive, indicating that the H30 sample undergoes a secondary magnetic transition as well [33].

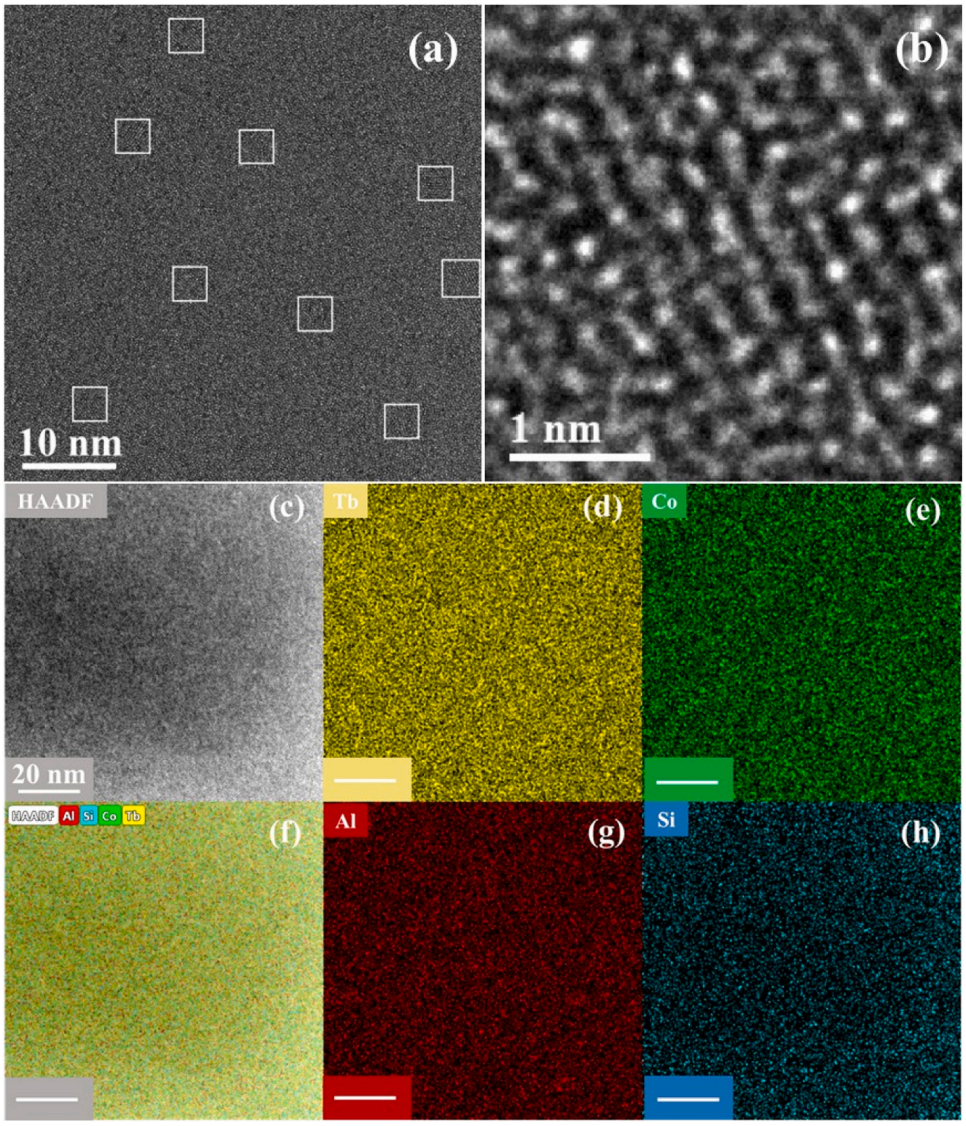

Fig. 5. (a) HRTEM image of the H30 sample. (b) An enlarged view of the white square in (a). (c) HAADF-TEM image of the H30 sample. (d-e) Corresponding of elemental mappings of the H30 sample.

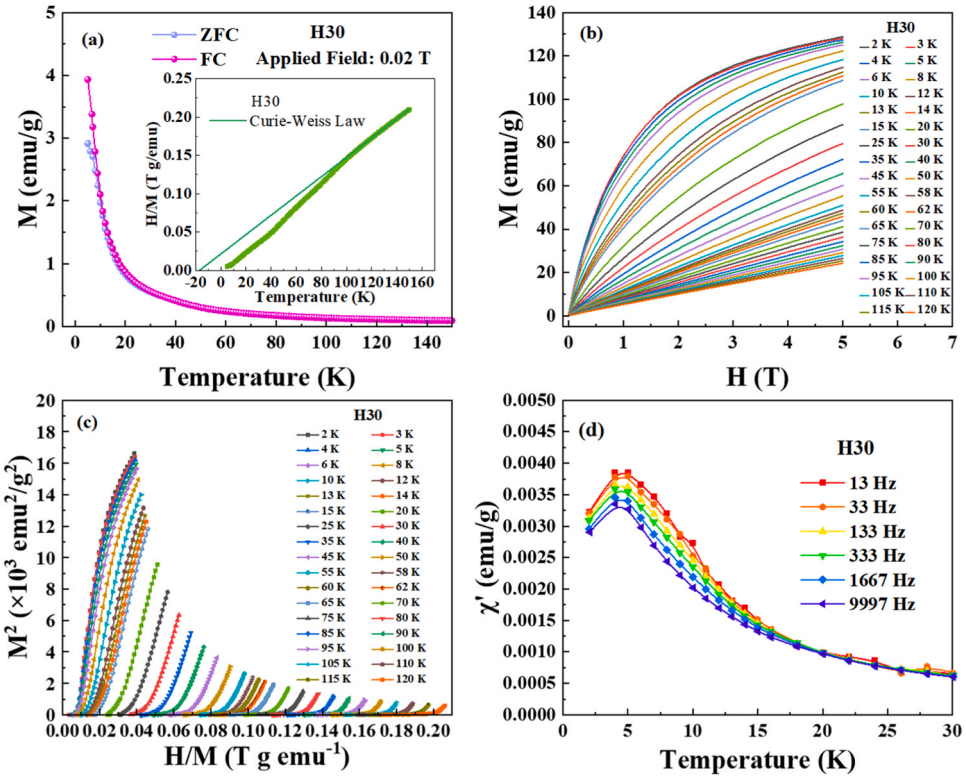

Fig. 6. (a) Magnetization curves of the H30 sample. The inset shows Curie-Weiss fitting of the magnetization curve. (b) Isothermal magnetization curves of the H30 sample. (c)Arrott plots calculated from M–H curves of the H30 sample. (d) The real part of susceptibility (χ) at frequencies ranging from 13 to 9997 Hz for the H30 sample.

Fig. 6(d) shows the real part of susceptibility (χ') at frequency ranging from 13 to 9997 Hz for the H30 sample. The peak temperature is almost constant ~ 5 K at different frequencies. This is different from the spin-glass-like behaviors observed in the Tb-based and Ho-based amorphous alloys [42–44], indicating the antiferromagnetic transition nature of TbCoAlSiH. In the GdTbDyCoAl and GdCoAl amorphous alloy, it was also found that the dominant exchange interaction after hydrogen absorption becomes antiferromagnetic [40,45].

The magnetic entropy change curves after hydrogen absorption are shown in Fig. 7(a). The peak position and shape of both curves remain almost the same under different field variations. The $-\Delta S_M^{max}$ of the H30 sample is enhanced from 7.5 $kg^{-1}K^{-1}$ (for the P30 sample) to 13.2 J $kg^{-1}K^{-1}$ at about 8 K an external field of 5 T, which is increased by 56.8 % by hydrogen absorption. The large increase of MCE originates from the formation of rare-earth hydrides as indicated from the HRTEM images and modulus distribution. This is different from the case of the La $(Fe_{0.88}Si_{0.12})_{13}H_{1.5}$ alloy, where hydrogen acts as the interstitial atoms [46]. Another important metric for magnetic cooling material applications is hysteresis loss. Fig. 7(b) compares the hysteresis loops of P30 and H30 samples at 2 K. The coercivity of the H30 sample decreases significantly from about 3734 Oe (for P30) to 160 Oe after hydrogen absorption. The above results show that hydrogenation is also an effective way to significantly reduce coercivity. Fig. 8 shows that the MCE of H30 is much larger than all other reported Tb-based, and typical soft Gd-based and Fe-based AMAs (the Dy-, Ho-based, Er-based AMSs are not included since they have a large coercivity at low temperatures) [40,47–56]. Besides, the maximum magnetic entropy changes were reported to be 9.62 J $kg^{-1}K^{-1}$ for $TbH_{1.92}$, 12.42 J $kg^{-1}K^{-1}$ for $TbH_{2.03}$ and 9.31 J $kg^{-1}K^{-1}$ for $TbH_{2.09}$ under 5 T [57], which are smaller that of present TbCoAlSiH alloy. This implies that the unique heterogeneous dual-phase structure plays a significant role on the enhancement of MCE, and the underlying mechanism needs to be further investigated. Finally, note that a similar enhanced MCE by hydrogen charging was reported in a Tb-based bulk AMA, where only a very narrow magnetic entropy peak arising from a few hydrides was observed and superimposed on the broad magnetic entropy change hump of the amorphous matrix [37]. This implies that the content of hydride plays an important impact on the magnetic transition and MCE performance.

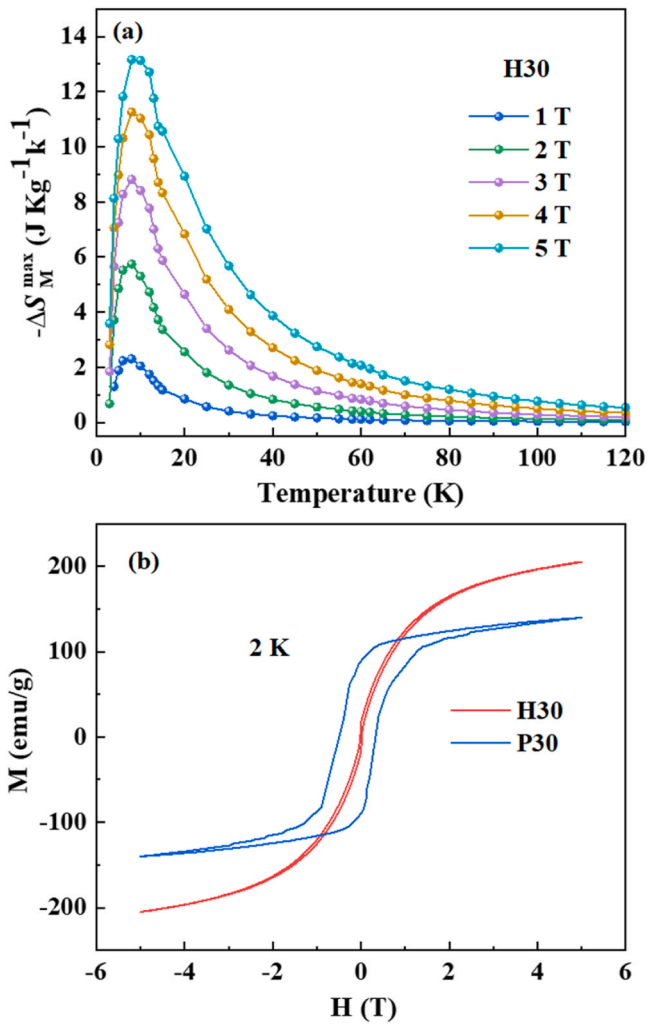

Fig. 7. (a) Temperature dependence of ΔS_M under the maximum applied field from 1 to 5 T of the H30 sample. (b) Magnetic hysteresis loops from −5–5 T at the temperature of 2 K for the P30 and H30 samples.

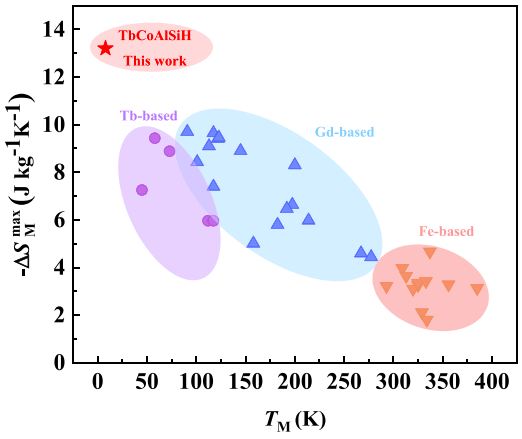

Fig. 8. A summary of T_M and $-\Delta S_M^{max}$ of TbCoAlSiH prepared in this work and other typical Fe-based, Gd-based and Fe-based amorphous alloys.

4. Conclusion

The effect of structure order and nanoscale hydride on the magnetocaloric performance of $Tb_{55}Co_{20}Al_{24}Si_1$ amorphous alloy powders were investigated. It is found that proper enhancement (excessive increase) of structure order can increase (decrease) the MCE performance of $Tb_{55}Co_{20}Al_{24}Si_1$. After hydrogenation, dual-phase structure with nanocrystalline hydrides (1–3 nm in size) embedded in the residual amorphous matrix is obtained. This unique heterogeneous structure has significant effects on the magnetocaloric properties and magnetic transition of $Tb_{55}Co_{20}Al_{24}Si_1$. The magnetic transition nature changes from ferromagnetic-paramagnetic to antiferromagnetic-paramagnetic transition after hydrogenation. And the maximum magnetic entropy change ($-\Delta S_M^{max}$) increased largely from 7.5 J kg^{-1}K^{-1} to 13.2 J kg^{-1}K^{-1}, indicating the potential of TbCoAlSiH alloy to be utilized in cryogenic magnetic cooling. The present results shed new light on the development of novel dual-phase magnetocaloric materials.

Author contributions

Q.L. and B.L.S. designed the research project; Q.Z.Y., J.X.C., M.J.Z. and H.Y.C. fabricated the samples and performed the magnetic and mechanical experiments and structural tests; H.R.Z and Y.Z. performed the hydrogenation experiments; Q.L. and B.L.S. conceptualized and supervised the research; Q.Z.Y. and Q.L. wrote the draft of the manuscript; Q.L. and B.L.S. contributed to the general discussion of the results. All authors commented on the manuscript.

CRediT authorship contribution statement

Haoyang Chang: Data curation. **Haoran Zhou:** Methodology. **Jingxian Cui:** Writing – review & editing, Formal analysis, Data curation. **Mingjie Zhang:** Methodology, Formal analysis. **Qianzi Yang:** Writing – review & editing, Writing – original draft, Methodology, Investigation, Formal analysis, Data curation. **Qiang Luo:** Writing – review & editing, Supervision, Methodology, Investigation, Funding acquisition, Conceptualization. **Yao Zhang:** Methodology. **Baolong Shen:** Writing – review & editing, Supervision, Project administration, Funding acquisition, Conceptualization.

Declaration of Competing Interest

The authors declare that they have no known competing financial interests or personal relationships that could have appeared to influence the work reported in this paper.

Acknowledgment

This work was supported by the National Natural Science Foundation of China (Grant Nos. 52231005 and 51971061) and Natural Science Foundation of Jiangsu Province (BK20221474).

References

[1] Z. Ma, X. Dong, Z. Zhang, L. Li, Achievement of promising cryogenic magnetocaloric performances in $La_{1-x}Pr_xFe_{12}B_6$ compounds, J. Mater. Sci. Tech. 92 (2021) 138–142, https://doi.org/10.1016/j.jmst.2021.02.055.
[2] B.G. Shen, J.R. Sun, F.X. Hu, H.W. Zhang, Z.H. Cheng, Recent progress in exploring magnetocaloric materials, Adv. Mater. 21 (2009) 4545–4564, https://doi.org/10.1002/adma.200901072.
[3] H. Hou, S. Qian, I. Takeuchi, Materials, physics and systems for multicaloric cooling, Nat. Rev. Mater. 7 (2022) 633–652, https://doi.org/10.1038/s41578-022-00428-x.
[4] V. Franco, J.S. Blazquez, J.J. Ipus, J.Y. Law, L.M. Moreno-Ramirez, A. Conde, Magnetocaloric effect: from materials research to refrigeration devices, Prog. Mater. Sci. 93 (2018) 112–232, https://doi.org/10.1016/j.pmatsci.2017.10.005.
[5] N. Terada, H. Mamiya, High-efficiency magnetic refrigeration using holmium, Nat. Commun. 12 (2021), https://doi.org/10.1038/s41467-021-21234-z.
[6] L. Li, M. Yan, Recent progresses in exploring the rare earth based intermetallic compounds for cryogenic magnetic refrigeration, J. Alloy. Compd. 823 (2020), https://doi.org/10.1016/j.jallcom.2020.153810.
[7] T. Gottschall, A. Gracia-Condal, M. Fries, A. Taubel, L. Pfeuffer, L. Manosa, A. Planes, K.P. Skokov, O. Gutfleisch, A multicaloric cooling cycle that exploits thermal hysteresis, Nat. Mater. 17 (2018) 929, https://doi.org/10.1038/s41563-018-0166-6.

[8] Y. Zhang, J. Zhu, S. Li, J. Wang, Z. Ren, Achievement of giant cryogenic refrigerant capacity in quinary rare-earths based high-entropy amorphous alloy, J. Mater. Sci. Tech. 102 (2022) 66–71, https://doi.org/10.1016/j.jmst.2021.06.028.

[9] X. Tang, H. Sepehri-Amin, N. Terada, A. Martin-Cid, I. Kurniawan, S. Kobayashi, Y. Kotani, H. Takeya, J. Lai, Y. Matsushita, T. Ohkubo, Y. Miura, T. Nakamura, K. Hono, Magnetic refrigeration material operating at a full temperature range required for hydrogen liquefaction, Nat. Commun. 13 (2022), https://doi.org/10.1038/s41467-022-29340-2.

[10] L.D. Griffith, Y. Mudryk, J. Slaughter, V.K. Pecharsky, Material-based figure of merit for caloric materials, J. Appl. Phys. 123 (2018), https://doi.org/10.1063/1.5004173.

[11] P. Xu, L. Hu, Z. Zhang, H. Wang, L. Li, Electronic structure, magnetic properties and magnetocaloric performance in rare earths (RE) based RE_2BaZnO_5 (RE = Gd, Dy, Ho, and Er) compounds, Acta Mater. 236 (2022), https://doi.org/10.1016/j.actamat.2022.118114.

[12] I. Park, S. Jeong, Development of the active magnetic regenerative refrigerator operating between 77 K and 20 K with the conduction cooled high temperature superconducting magnet, Cryogenics 88 (2017) 106–115, https://doi.org/10.1016/j.cryogenics.2017.09.008.

[13] A.O. Pecharsky, K.A. Gschneidner, V.K. Pecharsky, The giant magnetocaloric effect of optimally prepared $Gd_5Si_2Ge_2$, J. Appl. Phys. 93 (2003) 4722–4728, https://doi.org/10.1063/1.1558210.

[14] V.K. Pecharsky, K.A. Gschneidner, Giant magnetocaloric effect in $Gd_5(Si_2Ge_2)$, Phys. Rev. Lett. 78 (1997) 4494–4497, https://doi.org/10.1103/PhysRevLett.78.4494.

[15] M.E. Gruner, W. Keune, B. Roldan Cuenya, C. Weis, J. Landers, S.I. Makarov, D. Klar, M.Y. Hu, E.E. Alp, J. Zhao, M. Krautz, O. Gutfleisch, H. Wende, Element-resolved thermodynamics of magnetocaloric $LaFe_{13-x}Si_x$, Phys. Rev. Lett. 114 (2015), https://doi.org/10.1103/PhysRevLett.114.057202.

[16] F.X. Hu, B.G. Shen, J.R. Sun, Z.H. Cheng, G.H. Rao, X.X. Zhang, Influence of negative lattice expansion and metamagnetic transition on magnetic entropy change in the compound $LaFe_{11.4}Si_{1.6}$, Appl. Phys. Lett. 78 (2001) 3675–3677, https://doi.org/10.1063/1.1375836.

[17] H. Shen, H. Wang, J. Liu, F. Cao, F. Qin, D. Xing, D. Chen, Y. Liu, J. Sun, Enhanced magnetocaloric properties of melt-extracted GdAlCo metallic glass microwires, J. Magn. Magn. Mater. 372 (2014) 23–26, https://doi.org/10.1016/j.jmmm.2014.07.024.

[18] L. Liang, X. Hui, C.M. Zhang, G.L. Chen, A Dy-based bulk metallic glass with high thermal stability and excellent magnetocaloric properties, J. Alloy. Compd. 463 (2008) 30–33, https://doi.org/10.1016/j.jallcom.2007.09.041.

[19] S. Lu, M.B. Tang, L. Xia, Excellent magnetocaloric effect of a $Gd_{55}Al_{20}Co_{25}$ bulk metallic glass, Phys. B 406 (2011) 3398–3401, https://doi.org/10.1016/j.physb.2011.06.006.

[20] K. Loewe, J. Liu, K. Skokov, J.D. Moore, H. Sepehri-Amin, K. Hono, M. Katter, O. Gutfleisch, The effect of the thermal decomposition reaction on the mechanical and magnetocaloric properties of $La(Fe,Si,Co)_{13}$, Acta Mater. 60 (2012) 4268–4276, https://doi.org/10.1016/j.actamat.2012.04.027.

[21] B.Y. Song, Y.Q. Han, L. Gao, J. Cheng, C.L. Liu, J.H. Huang, Magnetocaloric effect and phase transformation of $LaFe_{11.0}M_{0.5}Si_{1.5}$ (M = Cu, Ni, Mg) alloys, J. Alloy. Compd. 965 (2023), https://doi.org/10.1016/j.jallcom.2023.171365.

[22] Y.F. Wang, F.X. Qin, Y. Luo, H. Wang, H.X. Peng, Tuning of magnetocaloric effect and optimization of scaling factor for $Gd_{55}Ni_{10}Co_{35}$ amorphous microwires, J. Alloy. Compd. 761 (2018) 1–7, https://doi.org/10.1016/j.jallcom.2018.05.152.

[23] H.F. Belliveau, Y.Y. Yu, Y. Luo, F.X. Qin, H. Wang, H.X. Shen, J.F. Sun, S.C. Yu, H. Srikanth, M.H. Phan, Improving mechanical and magnetocaloric responses of amorphous melt-extracted Gd-based microwires via nanocrystallization, J. Alloy. Compd. 692 (2017) 658–664, https://doi.org/10.1016/j.jallcom.2016.08.254.

[24] L. Xia, K.C. Chan, Enhanced magnetocaloric effect of a partially crystalline $Gd_{55}Al_{20}Ni_{25}$ bulk metallic glass, Solid. State Sci. 13 (2011) 2086–2089, https://doi.org/10.1016/j.solidstatesciences.2011.08.003.

[25] Q. Zheng, L. Zhang, J. Du, Magnetic entropy change in $Gd_{95}Fe_{2.8}Al_{2.2}$ amorphous/nanocrystalline ribbons, Scr. Mater. 130 (2017) 170–173, https://doi.org/10.1016/j.scriptamat.2016.11.041.

[26] H. Yin, J.Y. Law, Y. Huang, H. Shen, S. Jiang, S. Guo, V. Franco, J. Sun, Enhancing the magnetocaloric response of high-entropy metallic-glass by microstructural control, Sci. China Mater. 65 (2022) 1134–1142, https://doi.org/10.1007/s40843-021-1825-1.

[27] J.Q. Feng, Y.H. Liu, J.H. Sui, A.N. He, W.X. Xia, W.H. Wang, J.Q. Wang, J.T. Huo, Giant refrigerant capacity in Gd-based amorphous/nanocrsytalline composite fibers, Mater. Today Phys. 21 (2021), https://doi.org/10.1016/j.mtphys.2021.100528.

[28] Q. Luo, J. Cui, Z. Zhang, M. Han, B. Shen, Tuning nanoscale heterogeneity by non-affine thermal strain to modulate defect activation and maximize magnetocaloric effect of metallic glass, Mater. Des. 225 (2023), https://doi.org/10.1016/j.matdes.2022.111500.

[29] Q. Luo, B. Schwarz, N. Mattern, J. Shen, J. Eckert, Roles of hydrogenation, annealing and field in the structure and magnetic entropy change of Tb-based bulk metallic glasses, AIP Adv. 3 (2013), https://doi.org/10.1063/1.4797619.

[30] Q. Luo, W.H. Wang, Rare earth based bulk metallic glasses, J. NonCryst. 355 (2009) 759–775, https://doi.org/10.1016/j.jnoncrysol.2009.02.006.

[31] Q. Luo, B. Schwarz, N. Mattern, J. Eckert, Giant irreversible positive to large reversible negative magnetic entropy change evolution in Tb-based bulk metallic glass, Phys. Rev. B 82 (2010), https://doi.org/10.1103/PhysRevB.82.024204.

[32] Z. Zhang, Q. Luo, L. Shao, L. Xue, B. Chen, B. Shen, Tuning magnetocaloric effect of Gd-Co-Al-Si bulk metallic glass via controlling degree of structural order, J. Magn. Magn. Mater. 545 (2022), https://doi.org/10.1016/j.jmmm.2021.168769.

[33] J. Li, L. Xue, W. Yang, C. Yuan, J. Huo, B. Shen, Distinct spin glass behavior and excellent magnetocaloric effect in $Er_{20}Dy_{20}Co_{20}Al_{20}RE_{20}$ (RE = Gd, Tb and Tm) high-entropy bulk metallic glasses, Intermetallics 96 (2018) 90–93, https://doi.org/10.1016/j.intermet.2018.03.002.

[34] S.K. Banerjee, On a generalised approach to 1st and 2nd order magnetic transitions, Phys. Lett. 12 (1964) 16–17, https://doi.org/10.1016/0031-9163(64)91158-8.

[35] Q. Wang, L.L. Pan, B.Z. Tang, D. Ding, L. Xia, Outstanding magnetocaloric properties at ambient temperature of a $Fe_{88}La_4Ce_3B_5$ amorphous alloy, J. NonCryst. 580 (2022), https://doi.org/10.1016/j.jnoncrysol.2021.121394.

[36] J. Li, J.Y. Law, H. Ma, A. He, Q. Man, H. Men, J. Huo, C. Chang, X. Wang, R.-W. Li, Magnetocaloric effect in Fe-Tm-B-Nb metallic glasses near room temperature, J. NonCryst. 425 (2015) 114–117, https://doi.org/10.1016/j.jnoncrysol.2015.06.002.

[37] H. Fu, M. Zou, N.K. Singh, Modification of magnetic and magnetocaloric properties of Dy-Co-Al bulk metallic glass introduced by hydrogen, Appl. Phys. Lett. 97 (2010), https://doi.org/10.1063/1.3534794.

[38] N. Ismail, A. Gebert, M. Uhlemann, J. Eckert, L. Schultz, Effect of hydrogen on $Zr_{65}Cu_{17.5}Al_{7.5}Ni_{10}$ metallic glass, J. Alloy. Compd. 314 (2001) 170–176, https://doi.org/10.1016/S0925-8388(00)01211-1.

[39] W.E. Wallace, S.K. Malik, T. Takeshita, S.G. Sankar, D.M. Gualtieri, Magnetic-properties of hydrides of rare-earths and rare-earth intermetallics, J. Appl. Phys. 49 (1978) 1486–1491, https://doi.org/10.1063/1.324931.

[40] L.L. Shao, L. Xue, Q. Luo, K.B. Yin, Z.R. Yuan, M.Y. Zhu, T. Liang, Q.S. Zeng, L. T. Sun, B.L. Shen, Heterogeneous GdTbDyCoAl high-entropy alloy with distinctive magnetocaloric effect induced by hydrogenation, J. Mater. Sci. Tech. 109 (2022) 147–156, https://doi.org/10.1016/j.jmst.2021.08.076.

[41] W.G. Bos, K.H. Gayer, The rare earth hydrides, J. Nucl. Mater. 18 (1966) 1–30, https://doi.org/10.1016/0022-3115(66)90092-4.

[42] J. Du, Q. Zheng, E. Bruck, K.H.J. Buschow, W.B. Cui, W.J. Feng, Z.D. Zhang, Spin-glass behavior and magnetocaloric effect in Tb-based bulk metallic glass, J. Magn. Magn. Mater. 321 (2009) 413–417, https://doi.org/10.1016/j.jmmm.2008.09.034.

[43] Q. Luo, B. Schwarz, N. Mattern, J. Eckert, Magnetic ordering and slow dynamics in a Ho-based bulk metallic glass with moderate random magnetic anisotropy, J. Appl. Phys. 109 (2011), https://doi.org/10.1063/1.3594696.

[44] L. Xue, L.L. Shao, Q. Luo, B.L. Shen, $Gd_{25}RE_{25}Co_{25}Al_{25}$ (RE = Tb, Dy and Ho) high-entropy glassy alloys with distinct spin-glass behavior and good magnetocaloric effect, J. Alloy. Compd. 790 (2019) 633–639, https://doi.org/10.1016/j.jallcom.2019.03.210.

[45] L.L. Shao, Q. Luo, M.J. Zhang, L. Xue, J.X. Cui, Q.Z. Yang, H.B. Ke, Y. Zhang, B. L. Shen, W. Wang, Dual-phase nano-glass-hydrides overcome the strength-ductility trade-off and magnetocaloric bottlenecks of rare earth based amorphous alloys, Nat. Commun. 15 (2024), https://doi.org/10.1038/s41467-024-48531-7.

[46] S. Fujieda, Y. Hasegawa, A. Fujita, K. Fukamichi, Direct measurement of magnetocaloric effects in itinerant-electron metamagnets $La(Fe_xSi_{1-x})_{13}$ compounds and their hydrides, J. Magn. Magn. Mater. 272 (2004) 2365–2366, https://doi.org/10.1016/j.jmmm.2003.12.968.

[47] Q. Wang, D. Ding, B.Z. Tang, P. Yu, B. Xia, W.H. Li, L. Xia, A novel $Fe_{87}Pr_{11}B_2$ amorphous alloy with outstanding magnetocaloric properties near 325 K, Intermetallics 172 (2024) 108394, https://doi.org/10.1016/j.intermet.2024.108394.

[48] C.H. Wang, Q. Wang, B.Z. Tang, X. Zhou, D. Ding, L. Xia, Achieve good magnetocaloric response near the ambient temperature in a $Fe_{86}La_7B_5Ce_2$ amorphous ribbon, J. Magn. Magn. Mater. 547 (2022), https://doi.org/10.1016/j.jmmm.2021.168954.

[49] P. Yu, J.Z. Zhang, L. Xia, $Fe_{87}Zr_7B_4Co_2$ amorphous alloy with excellent magnetocaloric effect near room temperature, Intermetallics 95 (2018) 85–88, https://doi.org/10.1016/j.intermet.2018.01.019.

[50] L. Gan, L. Ma, B. Tang, D. Ding, L. Xia, Effect of Co substitution on the glass forming ability and magnetocaloric effect of $Fe_{88}Zr_8B_4$ amorphous alloys, Sci. China Phys. Mech. 60 (2017), https://doi.org/10.1007/s11433-017-9043-4.

[51] B. Huang, T.P. Ge, G.L. Liu, J.H. Luan, Q.F. He, Q.X. Yuan, W.X. Huang, K. Zhang, H.Y. Bai, C.H. Shek, C.T. Liu, Y. Yang, W.H. Wang, Density fluctuations with fractal order in metallic glasses detected by sib synchrotron X-ray nano-computed tomography, Acta Mater. 155 (2018) 69–79, https://doi.org/10.1016/j.actamat.2018.05.064.

[52] B. Schwarz, B. Podmilsak, N. Mattern, J. Eckert, Magnetocaloric effect in Gd-based $Gd_{60}Fe_xCo_{30-x}Al_{10}$ metallic glasses, J. Magn. Magn. Mater. 322 (2010) 2298–2303, https://doi.org/10.1016/j.jmmm.2010.02.029.

[53] Q. Luo, D.Q. Zhao, M.X. Pan, W.H. Wang, Magnetocaloric effect in Gd-based bulk metallic glasses, Appl. Phys. Lett. 89 (2006), https://doi.org/10.1063/1.2338770.

[54] Z. Zheng, X. Zhong, K. Su, H. Yu, Z. Liu, D. Zeng, Magnetic properties and large magnetocaloric effects in amorphous Gd-Al-Fe alloys for magnetic refrigeration, Sci. China Phys. Mech. 54 (2011) 1267–1270, https://doi.org/10.1007/s11433-011-4363-4.

[55] H. Fu, M. Zou, Magnetic and magnetocaloric properties of ternary Gd-Co-Al bulk metallic glasses, J. Alloy. Compd. 509 (2011) 4613–4616, https://doi.org/10.1016/j.jallcom.2011.01.126.

[56] J.T. Huo, L.S. Huo, H. Men, X.M. Wang, A. Inoue, J.Q. Wang, C.T. Chang, R.W. Li, The magnetocaloric effect of Gd-Tb-Dy-Al-M (M = Fe, Co and Ni) high-entropy bulk metallic glasses, Intermetallics 58 (2015) 31–35, https://doi.org/10.1016/j.intermet.2014.11.004.

[57] H. Drulis, A. Hackemer, L. Folcik, A. Zaleski, Magnetocaloric effect in terbium dihydrides: heat capacity measurements, Solid State Commun. 150 (2010) 164–167, https://doi.org/10.1016/j.ssc.2009.10.024.